Journal of Volcanology and Geothermal Research 474 (2026) 108603

Contents lists available at ScienceDirect

Journal of Volcanology and Geothermal Research

journal homepage: www.journals.elsevier.com/journal-of-volcanology-and-geothermal-research

Satellite data synergy for volcano monitoring: The 2022 Mauna Loa eruption

Ian T.W. Flynn [a,*], Shashank Bhushan [b,c], Scott Henderson [d,e], Claudia Corradino [f], Michael S. Ramsey [a], Evan R. Collins [a]

[a] Department of Geology and Environmental Science, University of Pittsburgh, 4107 O'Hara Street, Pittsburgh, PA 15260, USA
[b] Earth System Science Interdisciplinary Center, University of Maryland, 5825 University Research Ct suite 4001, College Park, MD 20740, USA
[c] Biospheric Sciences Laboratory, NASA Goddard Space Flight Center, 8800 Greenbelt Road, Greenbelt, MD 20771, USA
[d] eScience Institute, University of Washington, 3910 15th Ave NE, Seattle, WA 98195, USA
[e] Department of Earth and Space Sciences, University of Washington, 1707 NE Grant Lane, Seattle, WA 98195, USA
[f] Istituto Nazionale di Geofisica e Vulcanologia, Sezione di Catania, Osservatorio Etneo, 95125 Catania, Italy

ARTICLE INFO

Keywords:
Mauna Loa
Precursory activity
Machine learning
Lava flows
Satellite remote sensing
Lava flow thickness

ABSTRACT

The 2022 Mauna Loa eruption started on 27 November and ended on 10 December, lasting 13 days and was observed by several satellite instruments, operated by both commercial companies and government agencies. Here, we used these data for a multidisciplinary retrospective analysis of the entire eruption, including high-resolution satellite visible images to monitor the lava flow areal coverage rate, airborne LiDAR and orbital stereo-visible images to generate a flow thickness map, and thermal infrared data to perform a thermal time series analysis. Combining these different datasets provides a holistic view of the eruption. A measurable pre-eruption thermal increase was detected on 22 October 2022, approximately one month prior to eruption start. This thermal area within the northwest caldera wall is consistent with past fumarole activity in the area but also increased in temperature prior to the eruption. Following the eruption onset, the entire flow field covered an area of 35.7 km^2 with a bulk volume of 0.13 km^3. The largest lava flow had an average areal coverage rate of 0.27 km^2/day, with approximately 80% of it being emplaced in 48 h after the source vent became active. Following emplacement, the thickest part (>20 m) of the flow field took ~21 months to fully cool to background temperatures. Our analysis demonstrates the usefulness of satellite data synergy to monitor future pre-, syn-, and post-eruptive changes in effusive volcanic systems.

1. Introduction

Monitoring and responding to a volcanic eruption using satellite instrument data has become standard practice over the last several decades (Coppola et al., 2020; Francis and Rothery, 2000; Harris, 2013; Ramsey and Flynn, 2020; Ramsey and Harris, 2013). Higher resolution data from instruments on the Terra, Aqua, the Landsat and Sentinel series, and the Advanced Land Observation Satellite (ALOS) platforms are commonly used to investigate volcanic activity. These instruments are operated by government agencies such as the National Aeronautics and Space Administration (NASA), the European Space Agency (ESA), or the Japanese Aerospace Exploration Agency (JAXA). However, instruments operated by commercial companies (e.g., Airbus, ICEYE, Maxar/Vantor, and Planet) have increased the availability of high spatial and temporal visible near infrared (VNIR) and radar data, as well as data products (i.e., topography) derived from those data. Researchers' ability to access these datasets and incorporate them into studies has also increased through NASA's Commercial SmallSat Data Acquisition (CSDA) program (Maskey et al., 2021) and similar collaborative arrangements. These data provide new tools for volcanology such as detailed morphology retrieved from the higher spatial resolution data (e.g., Dai et al., 2024; Galetto et al., 2025a) and/or denser VNIR time series investigations retrieved from the higher temporal resolution data. Such studies have been performed at Etna (Dozzo et al., 2024), Fogo (Bagnardi et al., 2016), Fuego (Aldeghi et al., 2019), Niijima Fukutoku-Okanoba (Simurda et al., 2022), Piton de la Fournaise (Chevrel et al., 2023), and Tolbachik (Dai and Howat, 2017). Furthermore, application of new analysis tools, such as machine learning (ML), to existing archival

* Corresponding author.
E-mail address: iantwflynn@pitt.edu (I.T.W. Flynn).

https://doi.org/10.1016/j.jvolgeores.2026.108603
Received 9 October 2025; Received in revised form 27 February 2026; Accepted 20 March 2026
Available online 22 March 2026

data enables training for model assessment of new activity and its likelihood of being precursory to an eruption (Corradino et al., 2023; Ramsey et al., 2023). However, the analysis of any volcano is limited to the capabilities and frequency of the individual instruments that observe the activity or deposits, as well as the accessibility of those data to scientists. No single satellite dataset covers the full wavelength spectrum or full range of spatial/temporal resolutions, limiting their applications. Thus, combining satellite datasets can provide a more robust and complete interpretation of a volcanic eruption. The increase and availability of satellite datasets, both commercial and public sector, provides new monitoring and hazard response capabilities for volcano science and observatories. Here we demonstrate the synergistic use of these satellite data before, during, and after the 2022 Mauna Loa, Hawaiʻi eruption.

Beginning in September 2022, Mauna Loa experienced an increase in seismic activity, with notable activity beneath the caldera and Southwest Rift Zone (SWRZ) (Maher et al., 2023). On 27 November 2022 a fissure opened in the summit caldera, marking the start of the effusive phase of this eruption (Lynn et al., 2025). Lava flows were first emplaced within the summit caldera and towards the SWRZ (Fig. 1). However, on the morning of 28 November the activity migrated to the Northeast Rift Zone (NERZ) with multiple fissures opening and several producing fire fountaining. From 29 November through 9 December 2022, the eruption continued primarily from Fissure 3, producing a vent and an ~18 km long channelized lava flow (Fig. 1). An extended eruption from Fissure 3 became the primary hazard as longer flows could result in the Daniel K. Inouye Highway (Saddle Road), a major transportation route for residents between the eastern and western sides of the island, being covered and cut off. Fortunately, when all effusive activity ceased on 10 December 2022, the Fissure 3 flow stopped ~3 km from the Saddle Road. Our investigation focuses on a thermal time series analysis from 2020 through to the end of the eruption, lava flow areal coverage rates for flows originating from Fissure 3, post emplacement topography, area, and volume. We also investigate the syn- and post-eruption thermal evolution of the eruption and its products.

2. Data and methods

2.1. Thermal analysis

Thermal trend analysis utilized a ML based model (Corradino et al., 2023) trained with data from the automated spatiotemporal thermal anomaly detection (ASTAD) algorithm (Ramsey et al., 2023). The model is a convolutional neural network (CNN) with a UNET architecture that was applied to the 90 m/pixel thermal infrared (TIR) data from the Advanced Spaceborne Thermal Emission and Reflection radiometer (ASTER) instrument on the Terra satellite (Kahle et al., 1991). A five-

Table 1
Datasets used in the study.

Acquisition System	Data Type	Date (DD/MM/YY)
3DEP	LiDAR	30/01/2018–06/01/2020
PlanetScope	VNIR image	30/11/22
PlanetScope	VNIR image	01/12/22
Landsat 8	VNIR image	02/12/22
PlanetScope	VNIR image	05/12/22
PlanetScope	VNIR image	07/12/22
Sentinel 2	VNIR image	11/12/22
ASTER	TIR images	01/01/2020–31/12/25
WorldView-2/3	Panchromatic stereo images	01/08/2023 and 02/07/2023

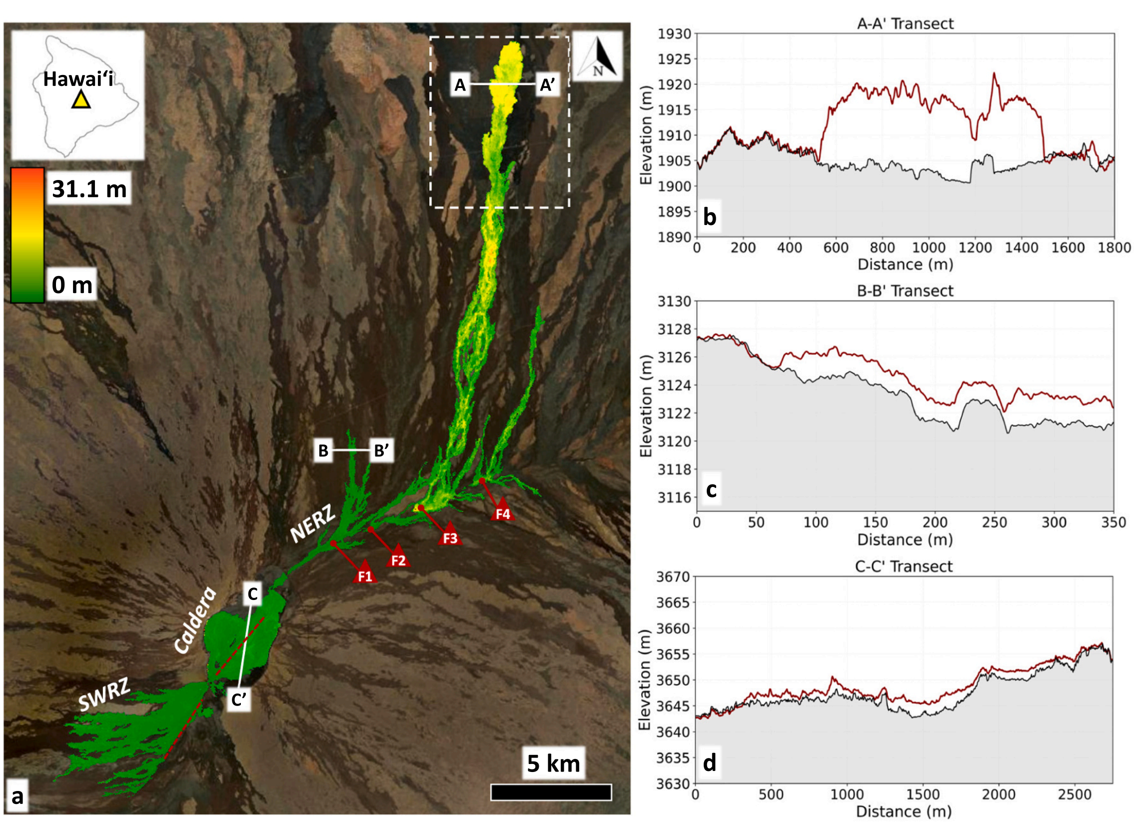

Fig. 1. The flow thickness map of the 2022 Mauna Loa eruption generated using post-event high resolution orbital optical stereo data and a pre-event LiDAR DEM. The inset shows the location of Mauna Loa – yellow triangle, and the white dashed rectangle indicates the region shown in Fig. 5. The red dashed lines and triangles show the locations of the caldera/rift zone fissures and the four fissure vents, respectively. The base map is created using the ArcPro World Imagery Mosaic (updated 1 August 2025, 0.5 m/pixel). The topographic transects, A – A', B – B′, and C – C′ are shown in (b), (c), and (d), respectively. For each of the profiles, the black and red lines indicate the pre- and post-eruption topography, respectively.

year period was analyzed starting in 2020 (Table 1). ASTAD is a statistical approach that uses the entire ASTER archive of both day and night TIR data accounting for varying cloud, temporal, seasonal, and elevation conditions to identify the accurate background temperature of each scene and any anomalous pixels with subtle ($1-2K$) temperatures above background (TAB). Prior studies using ASTER TIR data for thermal trending typically ignore the daytime scenes and those with any percentage of clouds in order to simplify the analysis (Gomez-Patron et al., 2025; Reath et al., 2019; Way et al., 2022). However, this can result in the removal of a significant percentage of scenes (≥ 50%) of the total archive in certain cases (Ramsey and Flynn, 2020), thus skewing results and potentially leading to poor training data for ML models. ASTAD uses a combined approach of data normalization and Gabor filtering (e.g., Gonzalez et al., 2010) to spatially cluster anomalous pixels in a similar way to how the human eye identifies clustered patterns of anomalies in TIR images. The normalization uses a morphological reconstruction to create a thermal intensity image. The pixel intensities are passed through a Gabor filter, which further highlights spatial edges and low intensity signals. Each pixel is weighted on both the intensity as well as spatial location thereby reducing outliers (possible false positives). Finally, from this intensity subset, pixels are identified as anomalies if they are above the TAB (see Ramsey et al., 2023 for further details). ASTAD-ML further enhances the original ASTAD performance because it learns spatial features from the ASTAD training data instead of the time consuming and explicitly programmed Gabor filtering.

ASTAD has been tested at Etna, Fuego, Kliuchevskoi, Lascar, and Popocatepetl to identify thermal trends (Ramsey et al., 2023). These results were later used by Corradino et al. (2023) as the labeled data to train the UNET CNN model. The ASTAD-ML model was then applied to a different volcano (Vulcano, Italy) and found to achieve a high accuracy (93%) with excellent generalization capabilities. For this analysis we applied the ASTAD-ML model to 295 L1T radiance ASTER TIR scenes from 1 January 2020 to 31 December 2025 (Table 1). The derivative of the heat flux running average is used to identify periods of thermal increase and flagged at points in time where this increase exceeds a certain threshold confidence value (Ramsey et al., 2023).

2.2. Flow front monitoring

We used four Planet SuperDove, one Landsat 8, and one Sentinel 2 image(s) to monitor the Fissure 3 channelized lava flow progression (Table 1). Planet SuperDove is a constellation of ~200 CubeSats, each with eight spectral bands (443–865 nm) in the VNIR, a spatial resolution of 3 m/pixel, and a temporal resolution of ~24 h. Planet data products are typically available to users within 24 h of acquisition. For this analysis we used the processed surface reflectance data product that includes geometric and radiometric corrections (Tu et al., 2022). Calibrated surface reflectance data from the Landsat 8 Operational Land Imager (OLI) and the Sentinel 2 Multispectral Instrument (MSI) were also incorporated into the flow front analysis (Table 1). The VNIR data from OLI (430–1380 nm) and MSI (~493 – ~833 nm) have a spatial resolution of 15 m/pixel and 10 m/pixel, respectively (Roy et al., 2014). The flow front monitoring rate was performed using the ArcGIS Pro software by measuring the observable surface area change over the number of days between observations.

2.3. DEM and elevation change map generation

The data used for the pre-eruption topographic reference map was produced by the National 3D Elevation Program (3DEP) program (Stoker, 2020) airborne light detection and ranging (LiDAR) surveys conducted between January 2018 and June 2020 (Table 1), with a spatial resolution of 1 m/pixel. The LiDAR digital elevation model (DEM) tiles were provided in NAD83 PA11 UTM Zone 5 N coordinate system (EPSG:6635) with geoid-based heights. We reprojected the DEM tiles into the WGS84 coordinate system with ellipsoid-based heights using a multi-step process. We first reprojected the DEM tiles into EPSG:6321 3D coordinate system using the National Oceanic and Atmospheric Administration's (NOAA) G2012B geoid model for Hawaiʻi and then applied Helmert transforms (e.g., Watson, 2006) for final conversion to UTM Zone 5 N coordinates with WGS84 ellipsoid heights in the G2139 realization. We mosaicked the reprojected DEM tiles to produce a final pre-event LiDAR DEM composite (see Henderson et al. (2026) for full processing details).

The post eruption topography data set was produced using three Maxar WorldView-2 (catalog ids: 10300100EB428000, 10300100EB76E500, 10300100EA132300, 10300100EB71A800) and WorldView-3 (catalog ids: 10400100878CFF00, 1040010088200700) stereo pairs collected on 2 July and 1 August 2023 (Table 1). We independently processed the panchromatic bands of each stereo pair using the open-source NASA Ames Stereo Pipeline (ASP) software (Beyer et al., 2018; Shean et al., 2016), version 3.5.0_alpha (Alexandrov et al., 2024) to derive three DEMs at 2 m/pixel horizontal resolution following the methods outlined in Bhushan et al. (2024). All DEMs were also produced in the G2139 realization of the WGS84 UTM Zone 5 N coordinate system to allow for direct comparison with the pre-event LiDAR DEM composite. We then co-registered the three optical image-derived DEMs to the pre-event LiDAR-derived reference DEM composite following (Nuth and Kääb., 2011) algorithm. We restricted the co-registration control points to surfaces that were not affected by the lava flow. We mosaicked the co-registered stereo DEMs into a single post-event DEM composite using the weighted average algorithm in ASP's DEM mosaic utility.

Finally, we estimated elevation change by subtracting the pre-event LiDAR DEM from the post-event optical DEM composite. We extracted the elevation change values over the lava flow path to produce the lava flow thickness maps. Points over areas not affected by lava flow were also used as check points to estimate the accuracy of the elevation change and lava flow thickness maps. Volumetric error was calculated following the methods described in Carr et al. (2019).

3. Results

3.1. Eruption thermal trends

The ASTER TIR sensor has been acquiring data for over 25 years and regularly images the volcanoes of Hawaiʻi on every day and night overpass providing an average of one scene per week. The ASTAD-ML results identified anomalous thermal features during the entire observation period corresponding to baseline thermal activity indicative of Mauna Loa (Fig. 2). A variety of thermal features that stand out from the background temperature trend have previously been noted in ASTER images collected from 2000 to 2010, including several elevated temperature locations in the caldera and along the rift zones (Patrick and Witzke, 2011).

On 22 October 2022, a pre-eruption subtle thermal increase above that of the longer-term persistent thermal features was identified within the Mauna Loa caldera by ASTAD-ML (Fig. 2). This increase in heat flux of <0.5 MW was during the same period when seismicity increased (Lynn et al., 2024) and could likely have been produced by a change in the hydrothermal system with higher degassing/heat flow from the fumaroles and existing caldera floor fissures. The concentration of pre-eruption thermal anomalies along the northwestern caldera wall (Fig. 3a) aligns with previously noted fumarole activity in the area (Casadevall and Hazlett, 1983; Patrick and Witzke, 2011). Specifically, the Oasis steam vent that was situated in the wall of Mokuʻāweoweo caldera identified in Casadevall and Hazlett (1983). The majority of thermally elevated pixels are associated with the caldera wall, however, several pixels overlap with the west caldera floor unit from Patrick and Witzke (2011), which is an ~230 m diameter area of alteration deposits that has previously been identified as having persistent temperatures above background. Notably, this cluster of pixels (Fig. 3a) are identified

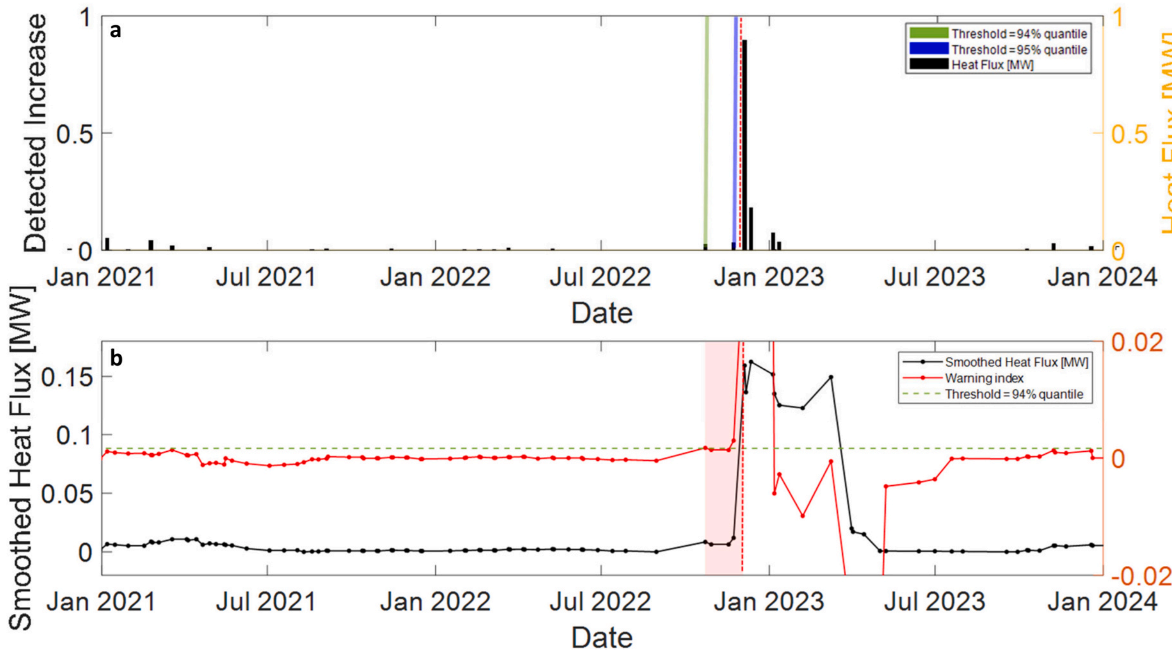

Fig. 2. (a) ASTER time series and pre-eruptive sequence using ASTAD-ML (Corradino et al., 2023) and (b) warning index (Ramsey et al., 2023). In (a) the red dashed line indicates the start of the eruption, the green and blue lines indicate a statistically significant increase in thermal activity for the 94% and 95% quartile, respectively. The heat flux is calculated based on the thermally elevated pixels identified by ASTAD-ML.

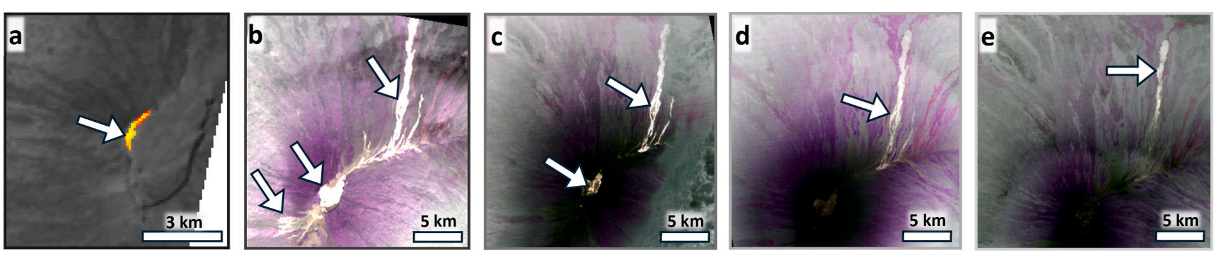

Fig. 3. Pre-, syn-, and post-eruption ASTER scenes. (a) Pre-eruption thermal activity identified by the ASTAD-ML within the caldera of Mauna Loa on 22 November 2022, daytime scene. Pixels in orange have elevated temperatures above the average background temperature; base image is ASTER Band 13. (b) Syn-eruption nighttime scene from 4 December 2022, displaying the entire flow field. Post-eruption nighttime scenes, (c) 6 February 2022, (d) 9 March 2023, and (e) 21 November 2023. Panels b-e are all displayed using bands 10–12-14 in RGB combination. White arrows indicate regions that are thermally elevated above background. All images are orientated with North to the top.

by the ML model as anomalous because they are above that of the long term thermally elevated zone. This area was clearly heating up prior to the eruption. A post-eruptive cooling phase at the summit is observed from the net decrease in the derivative signal observable from 11 December 2022 onward. The 11 December 2022 and 4 January 2023 points correspond to the existing flows and their heat flux released on those days (Fig. 2).

Two cloud-free ASTER TIR scenes, 4 December 2022 (daytime) and 6 December 2022 (nighttime), were acquired during the two week long eruption (Fig. 2). After the eruption ended, areas of all the lava flows remained thermally elevated above background until the end of January 2023, ~2 months after the eruption ended (Fig. 3). The first flows to cool to background temperature were those emplaced in the SWRZ and those from Fissures 1 and 2 in early February 2023, ~3 months after the eruption ended (Fig. 3c). The caldera and Fissure 4 flows were next to cool to background temperature ~ 4 months are the eruption ended in early March 2023 (Fig. 3d). The distal end of the channelized lava flow from Fissure 3 remained thermally elevated until 29 September 2024, ~21 months after the eruption ended (Fig. 3e). The maximum temperature values for the syn- and post-eruption periods (from 4 December 2022 to 14 April 2024) show an exponential decrease in temperature. This is consistent with the observations of the eruption using data from the Visible Infrared Imaging Radiometer Suite (VIRIS) (Aveni et al., 2025), which has a higher temporal (VIRIS daily and ASTER 3–16 days) but a lower spatial resolution (VIRIS 375 m/pixel and ASTER 90 m/pixel) than ASTER.

3.2. Mauna loa eruption: area, volume, and flow front areal coverage rate

The 2022 Mauna Loa eruption produced lava flows and vents covering an area of 35.7 km^2 and a volume of 0.13 ± 0.01 km^3 (Fig. 1a). The thickest regions of the flow (~20–30 $\pm$ 0.27 m) occur in the medial and distal regions of the Fissure 3 channelized lava flow (Fig. 1b). The lava flows in the SWRZ, caldera, and Fissures 1 and 2 have flow thicknesses $\leq 5 \pm 0.27$ m (Fig. 1c and d, Fig. 4). Lava flows from Fissure 4 are $\leq 10 \pm 0.27$ m thick throughout the entire flow field (Fig. 1a). Fissure 3 was the only fissure to produce a substantial constructed vent that covers an area of 0.04 km^2, has a volume of $5.24 \times 10^5 \pm 1.3 \times 10^4$ m^3. The vent walls have a maximum height of ~29 m and a maximum thickness of ~60 m. The surface texture and morphology of the vent suggest a spatter cone, with a comparable morphology to spatter cones formed during the 2021 Fagradalsfjall, Iceland, eruption (Flynn and

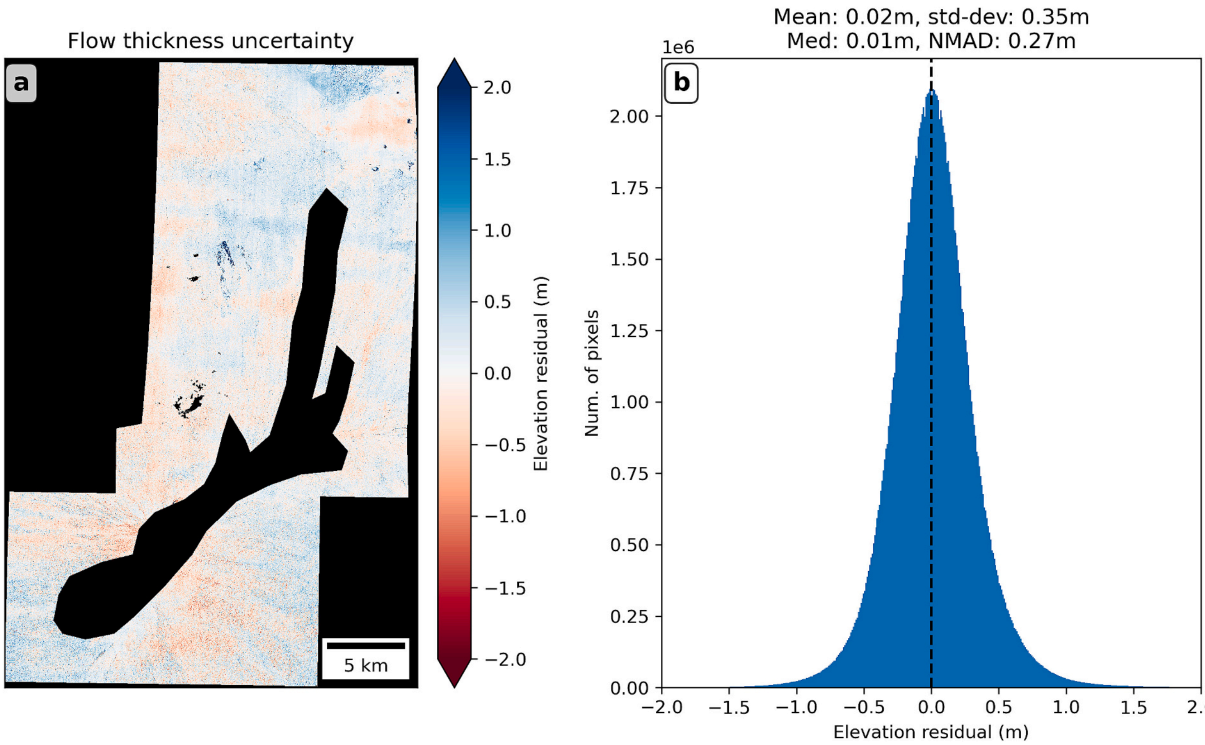

Fig. 4. Flow thickness uncertainty estimates. (a) Map-view plot of elevation residual between the post-event stereo DEM and the pre-event LIDAR DEM over areas not affected by the 2022 eruption lava flows. (b) Histogram of the elevation residual shown in (a), as well as the mean, median, standard deviation, and normalized median absolute deviation (NMAD) values.

Rader, 2024).

The first data observation of the Fissure 3 channelized lava flow used for this study occurred on 30 November 2022, two days after the eruption started in the NERZ (Fig. 5). From 28 November to 30

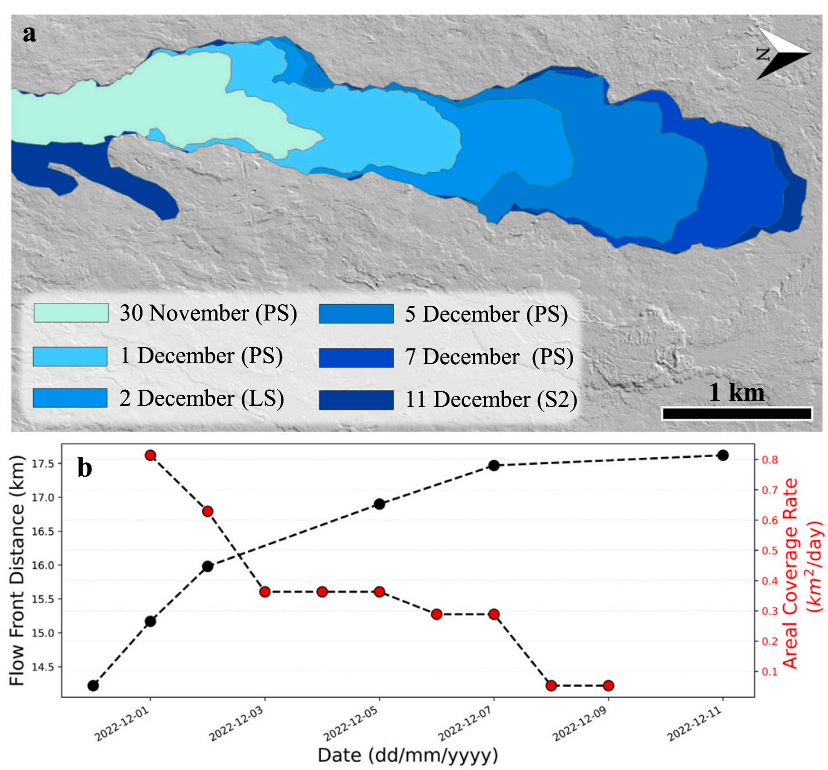

Fig. 5. (a) NERZ channelized lava flow front evolution obtained through Planet SuperDoves (PS), Landsat 8 (LS), and Sentinel 2 (S2) scenes (Table 1). The base map is a pre-eruption greyscale hillshade image from 3DEP (Table 1). (b) NERZ channelized lava flow front distance from the vent and calculated flow front areal coverage rate in km^2/day.

November the lava flow advanced from the Fissure 3 vent ∼14 km (∼80% of its full flow length) (Fig. 5). From 30 November until the end of the eruption, the flow advanced another ∼4 km, reaching its final length of ∼18 km on 10 December. During this eleven-day period, the average flow front areal coverage rate was 0.27 km^2/day. The largest areal coverage rate of 0.81 km^2/day (33.8 m/h) occurred from 30 November to 1 December (Fig. 5b). For the same observation period, 30 November to 1 December, a flow areal coverage rate of 24 m/h was reported (U.S. Geological Survey, 2022).

4. Discussion

We have demonstrated that combining multiple satellite datasets can be used to better monitor lava flow front progression, calculate volumetric change, and correlate thermal trends with physical volcanological features. This analysis was performed retrospectively; however, the Planet and Maxar/Vantor data are available to users rapidly (<24 h after acquisition) to incorporate into near real-time hazard response. As part of a future eruption, the workflow presented here could be used to monitor subtle thermal changes prior to an eruption, inform hazard response in near real time during an eruption, reduce the risk/need/cost of helicopter-based or uncrewed aerial vehicle (UAV) overflights, provide synoptic data not possible with drones, and/or calibrate numerical flow models. For example, the usefulness of incorporating satellite data into real-time lava flow hazard modeling was demonstrated for this eruption using the Lava2d model (Hyman et al., 2024). Chevrel et al. (2023) has also demonstrated the usefulness of incorporating Planet data (i.e., PlanetScope scenes) into the daily monitoring of lava flows for Piton de la Fournaise.

For this study, we also generated a flow thickness map after the eruption ended using Maxar WorldView-2/3 in-track steroscopic scenes (Table 1). However, this same DEM generation approach could be used with either Maxar/Vantor or Planet Skysat/Planetscope individual scenes with the proper viewing geometries during an active eruption to generate syn-eruption topographic datasets, if the scenes have the right viewing geometry and are not obscured by clouds or volcanic plumes. The presence of clouds or volcanic plumes is a common issue for generating DEMs using stereo-images over volcanoes (Flynn et al., 2024; Ramsey and Flynn, 2020). However, the frequency of these data greatly increases the likelihood of clear scenes. Furthermore, the requirement of specific viewing geometries can be addressed by tasking the satellite observations for in-track stereo imagery, an option offered by Planet Skysat, Maxar/Vantor and Airbus/CNES Pleiades-HR and has previously been used to generate DEMs at volcanoes around the world (Bhushan et al., 2021; Palaseanu-Lovejoy et al., 2019). The importance of acquiring syn-eruption DEMs for lava flow progression and hazard modeling has been demonstrated in recent studies (e.g., Pedersen et al., 2023; Tarquini et al., 2018). The evolving near-vent topography and lava emplacement may change flow pathways during an active eruption. This will result in discrepancies between initial model results and observed lava pathways, requiring frequent syn-eruption observations. Whether flow pathways change or not, accurate flow modeling of thinner flows still requires high-accuracy, high-resolution observation constraints (Flynn et al., 2023b; Roman and Lundgren, 2025). Very high resolution (VHR) optical stereo imagery offers the potential to address both requirements through rapid satellite tasking capabilities and the geometric precision, as demonstrated through our flow thickness products. For instance, our flow thickness products derived from VHR satellite stereo and airborne LiDAR DEMs achieve 27 cm NMAD and 35 cm standard deviation accuracy (Fig. 4). This elevation change accuracy is well within the 1 m requirement for flow modeling proposed in Roman and Lundgren (2025), even without post-processing smoothing filters (Richardson and Karlstrom, 2019). Given the potential rapid acquisition and availability of commercial satellite datasets that can be used to generate syn-eruption DEMs, this resource could be incorporated into future hazard response. Particularly in locations where DEMs generated from UAV or helicopter surveys may not be feasible daily because of costs or local conditions.

A distinct advantage of the Planet and Maxar/Vantor satellite constellations for active eruption monitoring is the high temporal resolution VNIR data acquisition. This comes from either the size of the satellite constellation (i.e., Planet) or from having targeted observations (i.e., Maxar/Vantor). Incorporating Planet data into our analysis enabled four additional observations of the flow front advance (Fig. 5 and Table 1). If we only utilized Landsat 8 and Sentinel 2 data, we would have just two observations of the flow front and would not have been able to measure variations in the flow front areal coverage rate (Fig. 5). Furthermore, we would not have been able to determine that ∼80% of the Fissure 3 channelized lava flow was emplaced in the first 48 h of the eruption starting in the NERZ. This highlights the advantages of satellite data synergy, and high spatial and temporal resolution datasets are for volcano monitoring and response.

4.1. *Thermal trends and flow thickness correlations*

The thermal trends derived from the ASTAD-ML model identified a period of increasing thermal output within the caldera prior to the eruption, during the same time as higher seismic activity. These temperatures dropped slightly before the eruption and then increased several times following its start (Fig. 2). After the eruption ended on 10 December, the lava flows cooled to background temperatures at different rates, correlating with the thickness of each flow unit. The thin flows (≤5 m) from the SWRZ and Fissure 1 and 2 cooled first, ∼3 months after the eruption ended. Next the caldera and Fissure 4 flows (∼5 m to ∼10 m) took ∼4 months to cool to background temperature. The thickest regions (∼20 m) of the flow from Fissure 3, medial and distal flow regions, remained thermally elevated for ∼21 months. This cooling trend is consistent with past studies that showed elevated thermal signatures as long as ∼40 years after the 1975 Great Tolbachik Fissure Eruption (GTFE), Russia, for a ∼ 50 m thick channelized lava flow (Ramsey et al., 2019; Wessels et al., 2005). However, the high spatial resolution of the post-eruption flow thickness map (Fig. 1), and moderate temporal and spatial resolution of ASTER thermal data enables the correlation of cooling rates to specific regions of the flow. This would not be possible with lower spatial resolution topography or thermal data. Measuring the cooling rates and flow thickness (even for flows that have stopped advancing) is important for safety and petrological studies. Furthermore, it can help constrain the modeled rates of lava flow cooling and potential observation of volcanic activity on other planets (e.g., Io and Venus) (Davies et al., 2005; Ganesh et al., 2024; Widemann et al., 2023).

4.2. *Lava flow emplacement timeline*

Combining multiple satellite datasets enabled high temporal observations of the Fissure 3 lava flow. This analysis would not have been possible without data provided through the NASA CSDA program. The areal coverage rate for the Fissure 3 lava flow supports previous observations that channelized lava flows primarily form in the early days of an eruption during periods of higher effusion (Gregg, 2017; Harris and Neri, 2002; Rowland et al., 2005). However, unlike previous studies we were able to quantify this observation with satellite datasets. Nearly 80% of the Fissure 3 NERZ channelized lava flow was emplaced within the first 48 h after the start of the eruption. The remainder was emplaced in the last eleven days of the eruption, and the areal coverage rate followed a nearly exponential decrease (Fig. 5). This pattern in flow areal coverage rate is also consistent with the observed exponential decrease volcanic radiative power for the eruption using VIIRS data (Aveni et al., 2025). In addition, the rapid emplacement of the Fissure 3 channelized lava flow is consistent with past observations of effusive eruptions that produced channelized flows at Mauna Loa (Riker et al., 2009). Our results build on the previous studies by providing a quantitative percentage of how much of an individual channelized lava flow is emplaced at the start of an eruption. Quantifying the emplacement rate of a terrestrial lava flow is important for future volcano monitoring (Ramsey et al., 2022) and hazard response protocols (Gottsmann et al., 2017). In addition, quantifying emplacement times for terrestrial channelized lava flows can help constrain our understanding of how channelized lava flows may be emplaced on other planets (e.g., Venus and Mars) (Flynn et al., 2022; Flynn et al., 2023a; Glaze et al., 2009; Widemann et al., 2023).

5. Conclusions

We have demonstrated the usefulness of satellite data synergy retrospectively to monitor an ongoing effusive eruption. Using data from existing commercial and publicly available orbital data, we identified an increase in thermal output prior to the start of the eruption, generated a lava flow thickness map, measured the flow front areal coverage rate for the Fissure 3 channelized lava flow, and investigated the thermal trends of those lava flows following cessation of the 2022 Mauna Loa eruption. The high temporal and spatial resolution of the commercial satellite datasets are uniquely suited for monitoring and responding to active eruptions. In contrast to prior studies that have used multiple datasets to investigate volcanic activity (e.g., Furtney et al., 2018; Galetto et al., 2025b; Ganci et al., 2020; Reath et al., 2016), we leverage commercial datasets combined with TIR data from public constellations to monitor the advancing lava flow front and correlate flow thickness with thermal trends.

Applying the ASTAD-ML model to part of the ASTER TIR time series identified a thermal increase precursory to the start of the eruption. This occurred during the same time as the increased seismicity at Mauna Loa perhaps indicating a change in the hydrothermal system below the caldera and a connection to the rising magma. The ASTER TIR sensor has now ended after an unprecedented 26 years in orbit, however there is a similar instrument with higher spatial resolution currently active on the International Space Station (ISS) – the Ecosystem Spaceborne Thermal Radiometer Experiment on Space Station (ECOSTRESS). Data from ECOSTRESS could be used to fill the TIR gap left by ASTER until new TIR missions are launched. These new missions include the Thermal infrared Imaging Satellite for High-resolution Natural resource Assessment (TRISHNA) mission by the French and Indian space agencies (Lagouarde et al., 2018), the Land Surface Temperature (LSTM) mission planned by the European Space Agency (ESA) as part of their Copernicus Sentinel system (Koetz et al., 2018), as well as the U.S. and Italy Surface Biology and Geology (SBG) mission (Thompson et al., 2023) and the Landsat Next missions (Portela et al., 2025). However, several of these U.S. missions are threatened by budget cuts and their launch dates are now uncertain. Upcoming missions from commercial companies seeking to provide high-resolution thermal imagery using a tasking-based approach (e.g., HydroSat and FireSat) might provide opportunities for improving our understanding of volcanic processes at finer spatial scales. However, these missions are still in development, and the yet-to-be scientifically vetted calibration quality of the new commercial offerings will determine their usability in rigorous time series analysis.

Complementing thermal observations, future topography time series data from the under-development Surface Topography and Vegetation mission concept (Donnellan et al., 2021) could provide updated topography maps before and after volcanic eruptions. Accurate and high spatial resolution topography data is critical for volcanic hazard modeling and quantifying eruptive volumes (e.g., Flynn et al., 2023b; Galetto et al., 2025b; Roman and Lundgren, 2025). Supplemented with more rapid topography measurements from tasked commercial acquisitions, this could potentially allow detailed studies of lava flow thickness progression and surface changes throughout the eruption cycle. This case study of the 2022 Mauna Loa eruption highlights the need to further develop integrated approaches leveraging both commercial and publicly available orbital datasets spanning thermal, topographic, and other remote sensing modalities for comprehensive volcanic monitoring and eruption response.

CRediT authorship contribution statement

Ian T.W. Flynn: Validation, Writing – review & editing, Writing – original draft, Visualization, Methodology, Investigation, Formal analysis, Conceptualization. **Shashank Bhushan:** Software, Visualization, Writing – review & editing, Writing – original draft, Resources, Methodology, Investigation, Formal analysis. **Scott Henderson:** Data curation, Methodology, Resources, Software, Writing – original draft, Writing – review & editing, Validation. **Claudia Corradino:** Data curation, Resources, Software, Validation, Writing – review & editing, Writing – original draft, Visualization, Investigation, Formal analysis. **Michael S. Ramsey:** Funding acquisition, Writing – original draft, Writing – review & editing, Supervision. **Evan R. Collins:** Software, Writing – original draft, Formal analysis.

Declaration of competing interest

The authors declare that they have no known competing financial interests or personal relationships that could have appeared to influence the work reported in this paper.

Acknowledgments

We appreciate the editorial support of Tobias Fishcher, and the constructive reviews from Matt Patrick and an anonymous reviewer. Thank you to Dave Hyman and Mike Zoeller for their assistance with acquiring pre-eruption topography data. Thank you to Matt Patrick, Hannah Dietterich, and Lis Gallant for helpful discussions regarding the 2022 Mauna Loa eruption. Shashank Bhushan was supported by the NASA Decadal Survey Incubation program (grant number NNH21ZDA001N-DSI).

Appendix A. Supplementary data

Supplementary data to this article can be found online at https://doi.org/10.1016/j.jvolgeores.2026.108603.

Data availability

All Planet data were supplied through their Education and Research program. This program is open to University-Affiliated students, faculty or researcher and provides access to PlanetScope and RapidEye imagery. The WorldView data was accessed through NASA's CSDA program utilizing NASA award 80NSSC19K0547, and can be obtained through the same mechanism by US-government federally funded researchers. The 3DEP LiDAR data is open source and archived at OpenTopography (Krishnan et al., 2011). The ASTER, Landsat, and Sentinel data are open source and archived at LP DAAC. The ASTAD-ML algorithm used in this study is available on GitHub (https://github.com/clacor89/ASTAD-ML/tree/main). The individual ASTER scene numbers used to generate Figure 2 can be found in Supplemental Table 1.

References

Aldeghi, A., Carn, S., Escobar-Wolf, R., Groppelli, G., 2019. Volcano monitoring from space using high-cadence planet CubeSat images applied to Fuego volcano, Guatemala. Remote Sens. 11 (18). https://doi.org/10.3390/rs11182151.

Alexandrov, O., ScottMcMichael, Broxton, Lundy, M., Beyer, R., Husmann, K., et al., 2024. NeoGeographyToolkit/StereoPipeline: 2024-11-25-daily-build. Zenodo. https://doi.org/10.5281/zenodo.14220272.

Aveni, S., Ganci, G., Harris, A.J.L., Coppola, D., 2025. Tracking Lava Flow Cooling from Space: Implications for Erupted volume Estimation and Cooling Mechanisms. Remote Sens. 17 (15), 2543. https://doi.org/10.3390/rs17152543.

Bagnardi, M., González, P.J., Hooper, A., 2016. High-resolution digital elevation model from tri-stereo Pleiades-1 satellite imagery for lava flow volume estimates at Fogo Volcano. Geophys. Res. Lett. 43 (12), 6267–6275. https://doi.org/10.1002/2016GL069457.

Beyer, R.A., Alexandrov, O., McMichael, S., 2018. The Ames Stereo Pipeline: NASA'S Open Source Software for Deriving and Processing Terrain Data. Earth and Space Science 5 (9), 537–548. https://doi.org/10.1029/2018EA000409.

Bhushan, S., Shean, D., Alexandrov, O., Henderson, S., 2021. Automated digital elevation model (DEM) generation from very-high-resolution Planet SkySat triplet stereo and video imagery. ISPRS J. Photogramm. Remote Sens. 173 (December 2020), 151–165. https://doi.org/10.1016/j.isprsjprs.2020.12.012.

Bhushan, S., Shean, D., Hu, J.Y.M., Guillet, G., Rounce, D.R., 2024. Deriving seasonal and annual surface mass balance for debris-covered glaciers from flow-corrected satellite stereo DEM time series. J. Glaciol. 70. https://doi.org/10.1017/jog.2024.57.

Carr, B.B., Clarke, A.B., Arrowsmith, J.R., Vanderkluysen, L., Dhanu, B.E., 2019. The emplacement of the active lava flow at Sinabung Volcano, Sumatra, Indonesia, documented by structure-from-motion photogrammetry. J. Volcanol. Geotherm. Res. 382, 164–172. https://doi.org/10.1016/j.jvolgeores.2018.02.004.

Casadevall, T., Hazlett, R., 1983. Thermal areas on Kilauea and Mauna Loa Volcanoes, Hawaii. J. Volcanol. Geotherm. Res. 16, 173–188. Retrieved from. https://archive.org/details/journal-of-volcanology-and-geothermal-research_1983-05_16_34.

Chevrel, M.O., Villeneuve, N., Grandin, R., Froger, J.-L., Coppola, D., Massimetti, F., et al., 2023. Lava flow daily monitoring: the case of the 19 September–5 October 2022 eruption at Piton de la Fournaise. Volcanica 6 (2), 391–404. https://doi.org/10.30909/vol.06.02.391404.

Coppola, D., Laiolo, M., Cigolini, C., Massimetti, F., Delle Donne, D., Ripepe, M., et al., 2020. Thermal Remote Sensing for Global Volcano monitoring: Experiences from the MIROVA System. Front. Earth Sci. 7. https://doi.org/10.3389/feart.2019.00362.

Corradino, C., Ramsey, M.S., Pailot-Bonnetat, S., Harris, A.J.L., Del Negro, C., 2023. Detection of subtle thermal anomalies: deep learning applied to the ASTER global volcano dataset. IEEE Trans. Geosci. Remote Sens. 61, 1–15. https://doi.org/10.1109/TGRS.2023.3241085.

Dai, C., Howat, I.M., 2017. Measuring lava flows with ArcticDEM: application to the 2012–2013 eruption of Tolbachik, Kamchatka. Geophys. Res. Lett. 44 (24), 12,133–12,140. https://doi.org/10.1002/2017GL075920.

Dai, C., Howat, I.M., van der Sluijs, J., Liljedahl, A.K., Higman, B., Freymueller, J.T., et al., 2024. Applications of ArcticDEM for measuring volcanic dynamics, landslides, retrogressive thaw slumps, snowdrifts, and vegetation heights. Sci. Rem. Sens. 9. https://doi.org/10.1016/j.srs.2024.100130.

Davies, A.G., Matson, D.L., Veeder, G.J., Johnson, T.V., Blaney, D.L., 2005. Post-solidification cooling and the age of Io's lava flows. Icarus 176 (1), 123–137. https://doi.org/10.1016/j.icarus.2005.01.015.

Donnellan, A., Harding, D., Lundgren, P., Wessels, K., Gardner, A., Simard, M., et al., 2021. Observing Earth's changing surface topography and vegetation structure: A framework for the decade. NASA Surface Topography and Vegetation Incubation Study 210.

Dozzo, M., Ganci, G., Lucchi, F., Scollo, S., 2024. Exploiting PlanetScope Imagery for Volcanic Deposits Mapping. Technologies 12 (2). https://doi.org/10.3390/technologies12020025.

Flynn, Ian T.W., Rader, E., 2024. Evidence of a Martian spatter cone south of Pavonis Mons. Icarus 424, 116286. https://doi.org/10.1016/j.icarus.2024.116286.

Flynn, I.T.W., Crown, D.A., Ramsey, M.S., 2022. Determining Emplacement Conditions and Vent Locations for Channelized Lava Flows Southwest of Arsia Mons. J. Geophys. Res. Planets 127 (11). https://doi.org/10.1029/2022JE007467.

Flynn, Ian.T.W., Chevrel, Magdalena.O., Ramsey, Michael.S., 2023a. Adaptation of a thermorheological lava flow model for Venus conditions. J. Geophys. Res. Planets 128 (7). https://doi.org/10.1029/2022JE007710.

Flynn, Ian T.W., Chevrel, M.O., Crown, D.A., Ramsey, M.S., 2023b. The effects of digital elevation model resolution on the PyFLOWGO thermorheological lava flow model. Environ. Model Softw. 167, 105768. https://doi.org/10.1016/j.envsoft.2023.105768.

Flynn, Ian T.W., Williams, D.B., Ramsey, M.S., 2024. Quantifying volumes of volcanic deposits using time-averaged ASTER digital elevation models. Sci. Rem. Sens. 10, 100179. https://doi.org/10.1016/j.srs.2024.100179.

Francis, P., Rothery, D., 2000. Remote sensing of active volcanoes. Annu. Rev. Earth Planet. Sci. 28 (1), 81–106.

Furtney, M.A., Pritchard, M.E., Biggs, J., Carn, S.A., Ebmeier, S.K., Jay, J.A., et al., 2018. Synthesizing multi-sensor, multi-satellite, multi-decadal datasets for global volcano monitoring. J. Volcanol. Geotherm. Res. 365, 38–56. https://doi.org/10.1016/j.jvolgeores.2018.10.002.

Galetto, F., Miller, S.M., Barris, R., Shevchenko, A.V., Pritchard, M.E., 2025a. The application of high resolution EarthDEM and ArcticDEM digital elevation models to detect and quantify volcanic activity: successes and challenges. Bull. Volcanol. 87 (7). https://doi.org/10.1007/s00445-025-01838-9.

Galetto, F., Reale, D., Coppola, D., Sansosti, E., Pritchard, M.E., 2025b. The application of remote sensing data (SAR, thermal and optical) and geodetic modeling to investigate the volcanic activity at Semeru Volcano (Indonesia). J. Geophys. Res. Solid Earth 130 (9). https://doi.org/10.1029/2025JB031428.

Ganci, G., Cappello, A., Bilotta, G., Del Negro, C., 2020. How the variety of satellite remote sensing data over volcanoes can assist hazard monitoring efforts: the 2011 eruption of Nabro volcano. Remote Sens. Environ. 236, 111426. https://doi.org/10.1016/j.rse.2019.111426. September 2019.

Ganesh, I., Flynn, I.T.W., Akins, A., Byrne, P.K., Carter, L.M., 2024. Lava Flow Cooling on Venus and Implications for Microwave Emission. LPI Contributions 3040, 1354.

Glaze, L.S., Baloga, S.M., Brent Garry, W., Fagents, S.A., Parcheta, C., 2009. A hybrid model for leveed lava flows: Implications for eruption styles on Mars. J. Geophys. Res. E: Planets 114 (7), 1–15. https://doi.org/10.1029/2008JE003278.

Gomez-Patron, A., Pritchard, M.E., Peng, X., Downes, A., Crothers, C., Valenza, J., et al., 2025. Are there thermal precursors to eruptions detectable by ASTER? Evaluating 22 years of global medium resolution satellite thermal observations at 200+ volcanoes. J. Geophys. Res. Solid Earth 130 (6). https://doi.org/10.1029/2024JB030427.

Gonzalez, R.C., Woods, R.E., Eddins, S.L., 2010. In: MathWorks (Ed.), Morphological Reconstruction. Digital Image Processing Using MATLAB.

Gottsmann, J., Komorowski, J.-C., Barclay, J., 2017. Volcanic unrest and pre-eruptive processes: A hazard and risk perspective. In: Volcanic Unrest. Springer, pp. 1–21.

Gregg, T.K.P., 2017. Patterns and processes: Subaerial lava flow morphologies: A review. J. Volcanol. Geotherm. Res. 342, 3–12. https://doi.org/10.1016/j.jvolgeores.2017.04.022.

Harris, A., 2013. Thermal Remote Sensing of Active Volcanoes: A User's Manual. Cambridge university press.

Harris, A.J.L., Neri, M., 2002. Volumetric observations during paroxysmal eruptions at Mount Etna: pressurized drainage of a shallow chamber or pulsed supply? J. Volcanol. Geotherm. Res. 116. https://doi.org/10.1016/S0377-0273(02)00212-3.

Henderson, S., Shean, D., Bhushan, S., Hayes, J., 2026. 3D CRS Transformation Resources (v0.1). Zenodo. https://doi.org/10.5281/zenodo.19210743.

Hyman, D.M.R., Dietterich, H.R., Gallant, E., Lynn, K.J., Zoeller, M.H., Patrick, M.R., et al., 2024. Real-time lava flow forecasting during the 2022 Mauna Loa eruption response. Bull. Volcanol. 87 (1), 3. https://doi.org/10.1007/s00445-024-01783-z.

Kahle, A.B., Palluconi, F.D., Hook, S.J., Realmuto, V.J., Bothwell, G., 1991. The advanced spaceborne thermal emission and reflectance radiometer (ASTER). Int. J. Imaging Syst. Technol. 3 (2), 144–156.

Koetz, B., Bastiaanssen, W., Berger, M., Defourney, P., Del Bello, U., Drusch, M., et al., 2018. High spatio-temporal resolution land surface temperature mission-a copernicus candidate mission in support of agricultural monitoring. In: Igarss 2018–2018 IEEE International Geoscience and Remote Sensing Symposium. IEEE, pp. 8160–8162.

Lagouarde, J.-P., Bhattacharya, B.K., Crébassol, P., Gamet, P., Babu, S.S., Boulet, G., et al., 2018. The Indian-French trishna mission: earth observation in the thermal infrared with high spatio-temporal resolution. In: IGARSS 2018–2018 IEEE International Geoscience and Remote Sensing Symposium, pp. 4078–4081. https://doi.org/10.1109/IGARSS.2018.8518720.

Lynn, K.J., Downs, D.T., Trusdell, F.A., Wieser, P.E., Rangel, B., McDade, B., et al., 2024. Triggering the 2022 eruption of Mauna Loa. Nat. Commun. 15 (1). https://doi.org/10.1038/s41467-024-52881-7.

Lynn, K.J., Gallant, E., Downs, D.T., Trusdell, F.A., 2025. Mauna Loa 2022—unrest, eruption, and outreach at the world's largest active volcano: preface to the special issue. Bull. Volcanol. 87 (8), 66. https://doi.org/10.1007/s00445-025-01842-z.

Maher, S.P., Dawson, P., Hotovec-Ellis, A., Thelen, W.A., Jolly, A., Bennington, N., et al., 2023. Characterizing and Locating Seismic Tremor during the 2022 Eruption of Mauna Loa Volcano, Hawai'i, with Network Covariance. The Seismic Record 3 (3), 228–238. https://doi.org/10.1785/0320230020.

Maskey, M., Hall, A., Murphy, K., Tucker, C., McCarty, W., Kaulfus, A., 2021. Commercial Smallsat Data Acquisition: Program Update. In: International Geoscience and Remote Sensing Symposium (IGARSS). Institute of Electrical and Electronics Engineers Inc., pp. 600–603. https://doi.org/10.1109/IGARSS47720.2021.9554702

Nuth, C., Kääb., 2011. Co-registration and bias corrections of satellite elevation data sets for quantifying glacier thickness change. Cryosphere 5 (1), 271–290. https://doi.org/10.5194/tc-5-271-2011.

Palaseanu-Lovejoy, M., Bisson, M., Spinetti, C., Buongiorno, M.F., Alexandrov, O., Cecere, T., 2019. High-resolution and accurate topography reconstruction of Mount Etna from pleiades satellite data. Remote Sens. 11 (24). https://doi.org/10.3390/rs11242983.

Patrick, M.R., Witzke, C.-N., 2011. Thermal Mapping of Hawaiian Volcanoes with ASTER Satellite Data. (No. 2011-5110). US Geological Survey.

Pedersen, G.B.M., Pfeffer, M.A., Barsotti, S., Tarquini, S., De'michieli Vitturi, M., Óladóttir, B.A., Prastarson, R.H., 2023. Lava flow hazard modeling during the 2021 Fagradalsfjall eruption, Iceland: applications of MrLavaLoba. Nat. Hazards Earth Syst. Sci. 23 (9), 3147–3168. https://doi.org/10.5194/nhess-23-3147-2023.

Portela, B., van der Werff, H., Hecker, C., van der Meijde, M., 2025. Landsat next current design for geological remote sensing: VNIR-SWIR-TIR data continuity and new opportunities. Sci. Rem. Sens. 12. https://doi.org/10.1016/j.srs.2025.100258.

Ramsey, M.S., Flynn, I.T.W., 2020. The spatial and spectral resolution of ASTER infrared image data: A paradigm shift in volcanological remote sensing. Remote Sens. 12 (4). https://doi.org/10.3390/rs12040738.

Ramsey, M.S., Harris, A.J.L., 2013. Volcanology 2020: how will thermal remote sensing of volcanic surface activity evolve over the next decade? J. Volcanol. Geotherm. Res. 249, 217–233. https://doi.org/10.1016/j.jvolgeores.2012.05.011.

Ramsey, M.S., Chevrel, M.O., Coppola, D., Harris, A.J.L., 2019. The influence of emissivity on the thermo-rheological modeling of the channelized lava flows at Tolbachik volcano. Ann. Geophys. 62 (2 Special Issue). https://doi.org/10.4401/ag-8077.

Ramsey, M.S., Harris, A.J.L., Watson, I.M., 2022. Volcanology 2030: will an orbital volcano observatory finally become a reality? Bull. Volcanol. 84 (1). https://doi.org/10.1007/s00445-021-01501-z.

Ramsey, M.S., Corradino, C., Thompson, J.O., Leggett, T.N., 2023. Statistical retrieval of volcanic activity in long time series orbital data: Implications for forecasting future activity. Remote Sens. Environ. 295, 113704. https://doi.org/10.1016/j.rse.2023.113704.

Reath, K.A., Ramsey, M.S., Dehn, J., Webley, P.W., 2016. Predicting eruptions from precursory activity using remote sensing data hybridization. J. Volcanol. Geotherm. Res. 321, 18–30. https://doi.org/10.1016/j.jvolgeores.2016.04.027.

Reath, K., Pritchard, M.E., Moruzzi, S., Alcott, A., Coppola, D., Pieri, D., 2019. The AVTOD (ASTER Volcanic thermal output Database) Latin America archive. J. Volcanol. Geotherm. Res. 376, 62–74. https://doi.org/10.1016/j.jvolgeores.2019.03.019.

Richardson, P., Karlstrom, L., 2019. The multi-scale influence of topography on lava flow morphology. Bull. Volcanol. 81 (4). https://doi.org/10.1007/s00445-019-1278-9.

Riker, J.M., Cashman, K.V., Kauahikaua, J.P., Montierth, C.M., 2009. The length of channelized lava flows: Insight from the 1859 eruption of Mauna Loa Volcano, Hawai'i. J. Volcanol. Geotherm. Res. 183 (3–4), 139–156. https://doi.org/10.1016/j.jvolgeores.2009.03.002.

Roman, A., Lundgren, P., 2025. Resolution and Error Constraints of Topographic Measurements for Accurate Lava Flow forecasting. Geophys. Res. Lett. 52 (21). https://doi.org/10.1029/2025GL115913.

Rowland, S.K., Garbeil, H., Harris, A.J.L., 2005. Lengths and hazards from channel-fed lava flows on Mauna Loa, Hawai'i, determined from thermal and downslope modeling with FLOWGO. Bull. Volcanol. 67 (7), 634–647. https://doi.org/10.1007/s00445-004-0399-x.

Roy, D.P., Wulder, M.A., Loveland, T.R., C.E., W., Allen, R.G., Anderson, M.C., et al., 2014. Landsat-8: science and product vision for terrestrial global change research. Remote Sens. Environ. 145, 154–172. https://doi.org/10.1016/j.rse.2014.02.001.

Shean, D.E., Alexandrov, O., Moratto, Z.M., Smith, B.E., Joughin, I.R., Porter, C., Morin, P., 2016. An automated, open-source pipeline for mass production of digital elevation models (DEMs) from very-high-resolution commercial stereo satellite imagery. ISPRS J. Photogramm. Remote Sens. 116, 101–117. https://doi.org/10.1016/j.isprsjprs.2016.03.012.

Simurda, C., Magruder, L.A., Markel, J., Garvin, J.B., Slayback, D.A., 2022. ICESat-2 applications for investigating emerging volcanoes. Geosciences 12 (1). https://doi.org/10.3390/geosciences12010040.

Stoker, J.M., 2020. Defining Technology Operational Readiness for the 3D Elevation Program—A Plan for Investment, Incubation, and Adoption. US Geological Survey.

Tarquini, S., De', M., Vitturi, M., Jensen, E.H., Pedersen, G.B.M., Barsotti, S., et al., 2018. Modeling lava flow propagation over a flat landscape by using MrLavaLoba: the case of the 2014–2015 eruption at Holuhraun, Iceland. Ann. Geophys. 62, 228. https://doi.org/10.4401/ag−7812.

Thompson, J.O., Williams, D.B., Ramsey, M.S., 2023. The expectations and prospects for quantitative volcanology in the upcoming Surface Biology and Geology (SBG) era. Earth Space Sci. 10 (5). https://doi.org/10.1029/2022EA002817.

Tu, Y.H., Johansen, K., Aragon, B., El Hajj, M.M., McCabe, M.F., 2022. The radiometric accuracy of the 8-band multi-spectral surface reflectance from the planet SuperDove constellation. Int. J. Appl. Earth Obs. Geoinf. 114. https://doi.org/10.1016/j.jag.2022.103035.

U.S. Geological Survey, 2022. HAWAIIAN VOLCANO OBSERVATORY STATUS REPORT. Retrieved from. https://volcanoes.usgs.gov/hans-public/notice/DOI-USGS-HVO-2022-11-30T18:05:22-08:00.

Watson, G.A., 2006. Computing Helmert transformations. J. Comput. Appl. Math. 197 (2), 387–394. https://doi.org/10.1016/j.cam.2005.06.047.

Way, L., Pritchard, M.E., Wike, L., Reath, K., Gunawan, H., Prambada, O., Syahbana, D., 2022. Detection of thermal features from space at Indonesian volcanoes from 2000 to 2020 using ASTER. J. Volcanol. Geotherm. Res. 430. https://doi.org/10.1016/j.jvolgeores.2022.107627.

Wessels, R., Ramsey, M., Dehn, J., Senyukov, S., 2005. Mapping elevated temperatures on a thirty-year-old basalt flow of New Tolbachik Volcano using satellite and ground-based thermal infrared. In: AGU fall meeting Abstracts, 2005. V31A-0605.

Widemann, T., Smrekar, S.E., Garvin, J.B., Straume-Lindner, A.G., Ocampo, A.C., Schulte, M.D., et al., 2023. Venus evolution through time: key science questions, selected mission concepts and future investigations. Space Sci. Rev. https://doi.org/10.1007/s11214-023-00992-w. Springer Science and Business Media B.V.